

# Height-integrated conductance and field-aligned current magnitudes evolve differently during a substorm

J. A. Carter<sup>1</sup>, S. E. Milan<sup>1</sup>, C. Forsyth<sup>2</sup>, M. E. Lester<sup>1</sup>, M.-T. Walach<sup>3</sup>, J. Gjerloev<sup>4</sup>, L. J. Paxton<sup>4</sup>, and B. J. Anderson<sup>4</sup>

<sup>1</sup>School of Physics and Astronomy, University of Leicester, University Road, Leicester, LE1 7RH, UK

<sup>2</sup>UCL Mullard Space Science Laboratory, Holmbury St. Mary, Dorking, Surrey, RH5 6NT, UK

<sup>3</sup>Physics Department, Lancaster University, Bailrigg, LA1 4YW, UK

<sup>4</sup>Applied Physics Laboratory, John Hopkins University, Laurel, Maryland 20723, U.S.A.

## Key Points:

- We track the progression of height-induced conductances, along with field-aligned currents, during substorms
- Low-latitude onsets exhibit the largest and longest-lived changes to height-integrated conductance
- Latitude of substorm onset has less control on field-aligned current magnitudes

---

Corresponding author: J. A. Carter, [jac48@le.ac.uk](mailto:jac48@le.ac.uk)

## Abstract

We examine the average evolution of precipitation-induced height-integrated conductances, along with field-aligned currents, in the nightside sector of the polar cap over the course of a substorm. Conductances are estimated from the average energy flux and mean energies derived from auroral emission data. Data are binned using a superposed epoch analysis on a normalised time grid based on the time between onset and recovery phase ( $\delta t$ ) of each contributing substorm. We also examine conductances using a fixed time binning of width 0.25 hr. We split the data set by magnetic latitude of onset. We find that the highest conductances are observed for substorms with onsets that occur between 63 and 65 degrees magnetic latitude, peaking at around 11 mho (Hall) and 4.8 mho (Pedersen). Substorms with onsets at higher magnetic latitudes show lower conductances and less variability. Changes in conductance over the course of a substorm appear primarily driven by changes (about 40% at onset) in the average energy flux, rather than the average energy of the precipitation. Average energies increase after onset slower than energy flux, later these energies decrease slowly for the lowest latitude onsets. No clear expansion of the main region 1 and region 2 field-aligned currents is observed. However, we do see an ordering of the current magnitudes with magnetic latitude of onset, particularly for region 1 downwards FAC in the morning sector. Peak current magnitudes occur slightly after or before the start of the recovery phase for the normalised and fixed-time grids.

## Plain Language Summary

Particles precipitate from Earth's magnetosphere into the upper ionosphere causing auroral emissions. A comparison of these auroral emissions, taken at different wavelengths, can be used to estimate the mean energy of the particles, as well as the flux, or number of precipitating particles in an area per unit time. From this mean energy and flux, we can estimate changes in the conductance of the ionosphere. Here, we examine how the conductance varies during the course of a substorm; when increased auroral emissions are seen suddenly on the nightside of the Earth. For this work we use imaging data from low-altitude spacecraft that give reasonable spatial coverage of the nightside ionosphere. We compare the changes in conductance over the course of an average substorm, to those seen in electrical currents that flow in the Earth's magnetosphere. The currents respond in a similar manner to the parameters derived from the auroral emissions.

## 1 Introduction

Deciphering the spatial and temporal variations in ionospheric conductances, under a variety of ambient conditions is of importance to the solar-terrestrial community (Denton et al., 2016). Knowledge of the conductance, is of particular importance, for example, when considering the coupling of component regions within magnetosphere and the thermosphere. Auroral imagers offer a method to estimate height-integrated conductances induced through particle precipitation simultaneously over large areas of the high-latitude polar cap region (Lam et al., 2019). There may be considerable differences between spatially precise, height-resolved conductances, and those presented in statistical maps (McGranaghan et al., 2015). However, statistical maps still have value as primers for global magnetospheric-ionospheric coupling models, particularly under extreme conditions (Mukhopadhyay et al., 2020). Parameterisation of height-integrated conductances at the dayside, under varying interplanetary magnetic field (IMF) and solar wind conditions, along with a simple parameterisation during an average substorm on the nightside, was presented in Carter et al. (2020). In this previous work, only the substorm phase relative to onset time was considered, using a superposed epoch analysis based on substorm onsets determined from the SuperMAG dataset (Newell & Gjerloev, 2011; Gjerloev, 2012). In this work we parameterise height-integrated conductances by substorm

phase and also by the magnetic latitude of substorm onset, as this is known to control substorm intensity (Milan et al., 2009). We also consider the evolution of these conductances with respect to distributions of field-aligned currents (FACs), which are an integral component of the magnetosphere-ionosphere coupled system.

Lester et al. (1996) examined Hall and Pedersen conductances during an individual substorm using an incoherent scatter radar. They found that the implied mean energy of the incoming precipitation varied during the progression of the substorm, which involved two expansion phases. At onset, the conductances were seen to increase to exceptionally high values of approximately 77 mho and 26 mho for Hall and Pedersen conductances respectively, whereas the mean energy remained constant. The second expansion phase showed a marked increase in mean energy, which was then doubled during the recovery phase. The authors suggested that the variations in mean energy were due to changes in acceleration processes in the magnetotail during the phase of a substorm, although observational effects from the radar are not discounted.

FACs in the Earth’s magnetosphere respond to the substorm cycle in a variety of ways. The main region 1 and region 2 FAC distributions expand quickly to lower latitudes in the growth phase, and simultaneously increases are seen in both region 1 and region 2 current magnitudes, although the increase is larger for region 1 (Coxon et al., 2014). The FAC latitude and magnitudes recover within about 20 mins. Asymmetries in the response of the FACs at onset are observed associated with the sign of the IMF  $B_Y$  component (Milan et al., 2018).

This paper is laid out as follows. In Section 2 we describe the data sets used to derive Pedersen and Hall height-integrated conductance values from observations of auroral emissions, FACs, and the substorm list on which we based our superposed epoch analysis. Here we also describe both a substorm-expansion phase binning and a fixed-time binning used for the superposed epoch analysis. We compare and discuss distributions of mean energy, mean energy flux, Pedersen and Hall height-integrated conductances in relation to the FACs during the progress of an average substorm in Section 3. We conclude in Section 4.

## 2 Data

We use a superposed epoch analysis of substorm phase to parameterise the other datasets described below. This study uses a modified Substorm Onsets and Phases from Indices of the Electrojet (SOPHIE) list from (Forsyth et al., 2015) which had been constructed from SuperMAG data and covers the years 2005 until 2019. This list is of those substorms with an expansion phase threshold with the SML index  $< -75$  nT, where the SML indices originate from SuperMAG (Gjerloev, 2012). This modified SOPHIE list contained the start of the expansion and recovery phases, plus the MLT and magnetic latitude locations for each substorm onset. We take the start of the expansion phase as the onset time. For this analysis, we only include substorm onsets that occurred between 18h MLT and 06h MLT, which we parameterise by onset latitude. We only used isolated substorms, i.e. those onsets that were preceded by a growth phase and followed by a recovery phase. This is to avoid multiple intensifications without an interim recovery period, and although these occur rarely (1% of time) (Milan et al., 2021), their effects could be large. The onset latitude bin boundaries were chosen to give good coverage of at least several hundreds of onsets per bin for the statistical analysis, with bins with a width of 2 degrees starting from  $63^\circ$ , apart from the bins at the extremes of the range. As in the study of Carter et al. (2020), substorm phases are taken at set intervals before and after onset. We define  $\delta t$  as the time period between onset and the start of the recovery phase for each contributing substorm. The expansion and recovery phase starts are given in the supplementary material of Forsyth et al. (2015). The duration of each substorm is not defined in this list. We use a step size of  $0.25 \delta t$  over the course of a substorm in

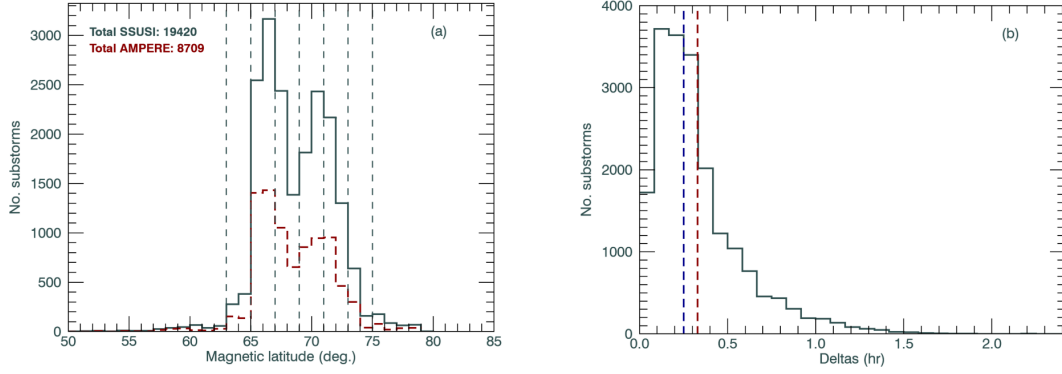


**Figure 1.** Statistics of the substorm onsets used in this analysis. Plot (a): A histogram of substorm onset latitudes from the (Forsyth et al., 2015) during the SSUSI (gray) and the shorter, but superimposed AMPERE (red) data periods. Dashed vertical lines indicate the boundaries used for the latitude selection in this analysis. Plot (b): A histogram of all  $\delta t$ , defined as the interval between the start of the substorm expansion and recovery phase (E-R) from the (Forsyth et al., 2015) list. The mean and median  $\delta t$  values are marked by the red and blue vertical dashed lines, respectively.

our analysis below. We also examine the behavior over an average substorm by using a time bin of a fixed width of 0.25 hrs.

In Fig. 1 we plot a histogram of substorm onset latitudes used in this study, along with a histogram of the  $\delta t$  intervals. Histograms for onset magnetic latitudes occurring during both the SSUSI (gray line) and AMPERE (red dashed line) data ranges are shown in plot (a), and a histogram of  $\delta t$  is shown in plot (b). The mean  $\delta t$  value is 0.32 hr, or 19.8 min. The minimum  $\delta t$  used in this analysis was 2 min.

Later in this paper we present Pedersen and Hall height-integrated conductances derived from auroral emissions data obtained by the Special Sensor Ultraviolet Spectrographic Imager (SSUSI) (Paxton & Anderson, 1992; Paxton & Zhang, 2016) on board three Defense Meteorological Satellite Programme (DMSP) spacecraft. We calculate the conductances from data products produced by the SSUSI team, and we describe these calculations and data products fully in Carter et al. (2020). However in summary, the conductances are calculated from the mean energy and mean energy flux of the incoming precipitating particles, which are assumed to be electrons, derived from Lyman-Birge-Hopfield (LBH) long (165-180 nm) and short band (140-150 nm) radiances. We use SSUSI data from the Southern Hemisphere in this paper, as we have good coverage of the mid-night local time sectors for all three DMSP spacecraft. The data originates from all available SSUSI files in the time period from 1 January 2005 to 31 December 2016 for F16, from 11 December 2006 to 4 August 2017 for F17, and from 17 November 2009 to 31 December 2017 for F18.

The calculation proceeded as follows. From the mean energy ( $E_0$ , in units of keV) and mean energy flux ( $Q$ , in units of  $\text{erg cm}^{-2} \text{s}^{-1}$ ), the height-integrated Pedersen ( $\Sigma_P$ ) and Hall ( $\Sigma_H$ ) conductances can be calculated per pixel, via the empirical expressions found in Robinson et al. (1987), and as shown in equations 1 and 2.

$$\Sigma_P = \frac{40E_0}{16 + E_0^2} \sqrt{Q} \quad (1)$$



$$\Sigma_H = 0.45(E_0^{0.85})\Sigma_P \quad (2)$$

To make a set of conductance maps, at each UT-stamped pixel at a given projected magnetic local time and magnetic latitude, the value of  $E_0$  and  $Q$  are considered separately from each contributing DMSP satellite, and used to calculate the Hall and Pedersen height-integrated conductances for that particular pixel. The conductances are then averaged at a given pixel to provide a series of images showing the average nightside spatial distribution of conductance at each substorm time step, whether fixed or related to  $\delta t$ , and for each latitude bin.

In this work we use SSUSI data products of mean energy and mean energy flux. These have been calculated based on the assumption of a Gaussian profile for the incoming particle precipitation energy distribution. Maxwellian and Gaussian distributions will have the same characteristic energy, but different mean energies (Robinson et al., 1987). Applying Eqn. 1 to an average energy flux of  $5.2 \text{ erg cm}^{-2} \text{ s}^{-1}$  and an average mean energy of 5.8 keV over the entire SSUSI data set used in this work, the Gaussian assumption would overestimate the height-integrated conductance at 10.7 mho compared to 7.0 mho for a Maxwellian distribution, see Fig. 2. Parity between distributions occurs for a characteristic energy of 2.85 keV, below which the Maxwellian assumption would overestimate the height-integrated conductance as compared to the Gaussian assumption. We present the calculated conductances as well as the behavior of  $E_0$  and  $Q$  in Section ??.

The auroral-derived products are accompanied by patterns of FACs, obtained from the Active Magnetosphere and Planetary Electrodynamics Response Experiment (AMPERE) (Anderson et al., 2000; Waters et al., 2001). The FACs have been organised with respect to substorm latitude and substorm phase in the same way as the spatial distributions of  $E_0$ ,  $Q$ , and conductance as described above. Contributing AMPERE data spans the period 1 January 2010 to 31 December 2016, which was available at the time of processing. Only current densities over  $0.1 \mu\text{A m}^{-2}$  are included to avoid including spurious low current density values that result from the AMPERE data processing technique, similar to the threshold used in Clausen et al. (2012).

### 3 Results and Discussion

In Fig. 3, we plot an example series of images showing the nightside spatial distribution of height-integrated Pedersen conductance (purple color scale), ordered by substorm phase along with contours of the FAC distribution at each phase. We overplot contours of upwards and downwards FAC distributions, colored red and blue respectively, at intervals of  $0.05 \mu\text{A m}^{-2}$ . This figure is plotted for the example magnetic latitude substorm onset bin of  $63^\circ$  to  $65^\circ$  degrees. In Fig. 4, in a similar format as the previous figure and again for the example magnetic latitude substorm onset bin of  $63^\circ$  to  $65^\circ$  degrees, we plot a set of differences image (purple-green color scale) showing the change in the conductance from the previous phase time step, expressed as a percentage. In these figures, the conductance begins to increase at onset at latitudes above 70 degrees and in MLT sectors just after local midnight. By  $0.5 \delta t$ , increases in conductance occur across many MLT and magnetic latitudes. Conductances begin to reduce at lower latitudes at  $0.75 \delta t$ , before starting to reduce at higher latitudes from  $1.00 \delta t$ . By  $1.25 \delta t$ , i.e. into the early part of the recovery phase, changes in conductance are seen at the edges of the main auroral oval, suggesting that dramatic differences in conductances here may be due to rapid changes to the auroral oval resulting in large percentage changes, or possibly artifacts of the averaging technique involving low numbers of contributing pixels, or less likely due to transient auroral events such as transpolar arcs which have not been screened for here. Clearer evidence of increased conductance at onset was observed when the magnetic latitude of substorm onset was not examined, as in Fig. 5 of Carter et al. (2020).

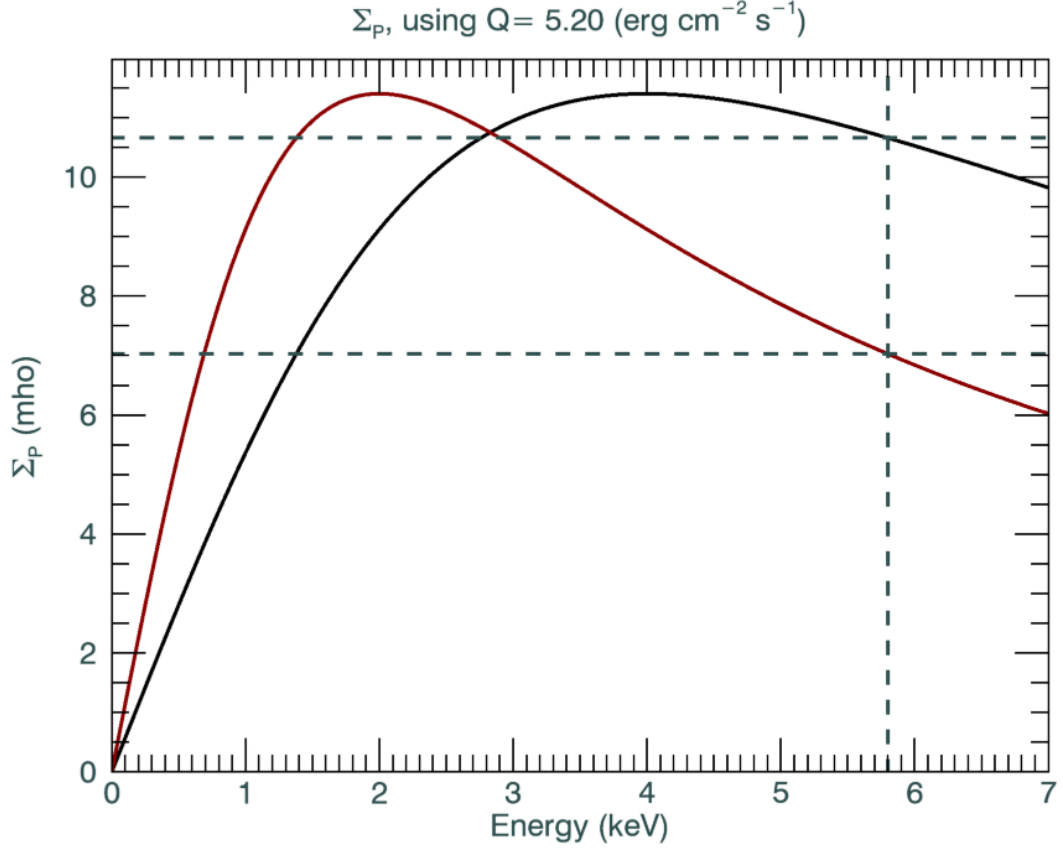


**Figure 2.** Height-integrated Pedersen conductances calculated using Eqn. 1 by assumed characteristic energy of the incoming particle precipitation, using the average mean energy flux of the SSUSI data set used in this work. This is calculated for a Maxwellian (red) or Gaussian (gray) distribution. Dashed lines indicate the average mean energy of the SSUSI data set.

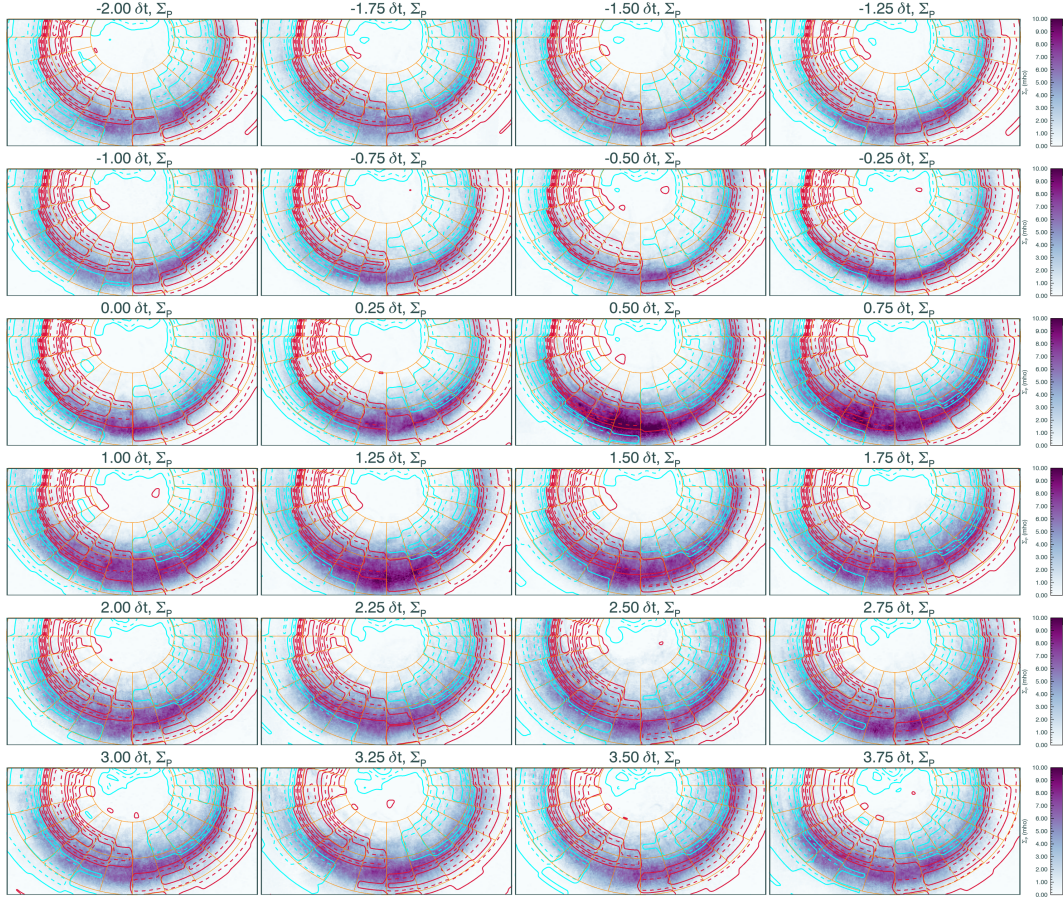


**Figure 3.** A series of images showing the nightside spatial distribution of height-integrated Pedersen conductance by substorm phase, for substorm onsets that occur between  $63^\circ$  to  $65^\circ$  degrees magnetic latitude. Each image is plotted on a magnetic-latitude, magnetic local time grid, with midnight to the bottom of each panel. On each panel we plot contours of the accompanying FAC distributions. Red contours are for upwards currents and blue contours are for downwards currents. Contours are plotted at intervals of  $0.05 \mu\text{A m}^{-2}$ .

FAC contours show little change in position throughout the substorm. The technique employed here has smeared out the subtle approximately 1-degree latitudinal changes seen in FAC distributions in magnetic latitude, that are seen on a case to case basis (Coxon et al., 2014). However, evolution of the FACs over the course of a substorm are observed here, which we present later in this section.

In Fig. 5 we plot average  $E_0$  and  $Q$  by MLT sector for a selection of MLTs,  $r$  the course of a substorm, for both the variable  $\delta t$  binning (top row), and a fixed time grid (bottom row). We observe the largest parameter values in all cases for the MLT = 23 hr sector ( $\approx 4.3 \text{ keV}$ , and  $\approx 6.8 \text{ ergs cm}^{-2} \text{ s}^{-1}$ ). The lowest peak values for each variable are found at the extreme east and west edges of the selected MLTs, which peak below  $4 \text{ keV}$  and below  $4 \text{ ergs cm}^{-2} \text{ s}^{-1}$ , consistent with the literature, e.g. Walach et al. (2017). Almost all  $E_0$  increase simultaneously after onset, with a slight delay to the east and west. We do not see a clear faster change in  $E_0$  eastwards, towards MLT = 02 hr, as compared to a slower expansion westwards to MLT = 21 hr, as implied by the work of Gjerloev et al. (2007). The mean energy flux  $Q$  rises sharply at onset for the fixed time binning, for all MLT sectors, whereas this is somewhat smeared out for the  $\delta t$  based grid.  $Q$  in the



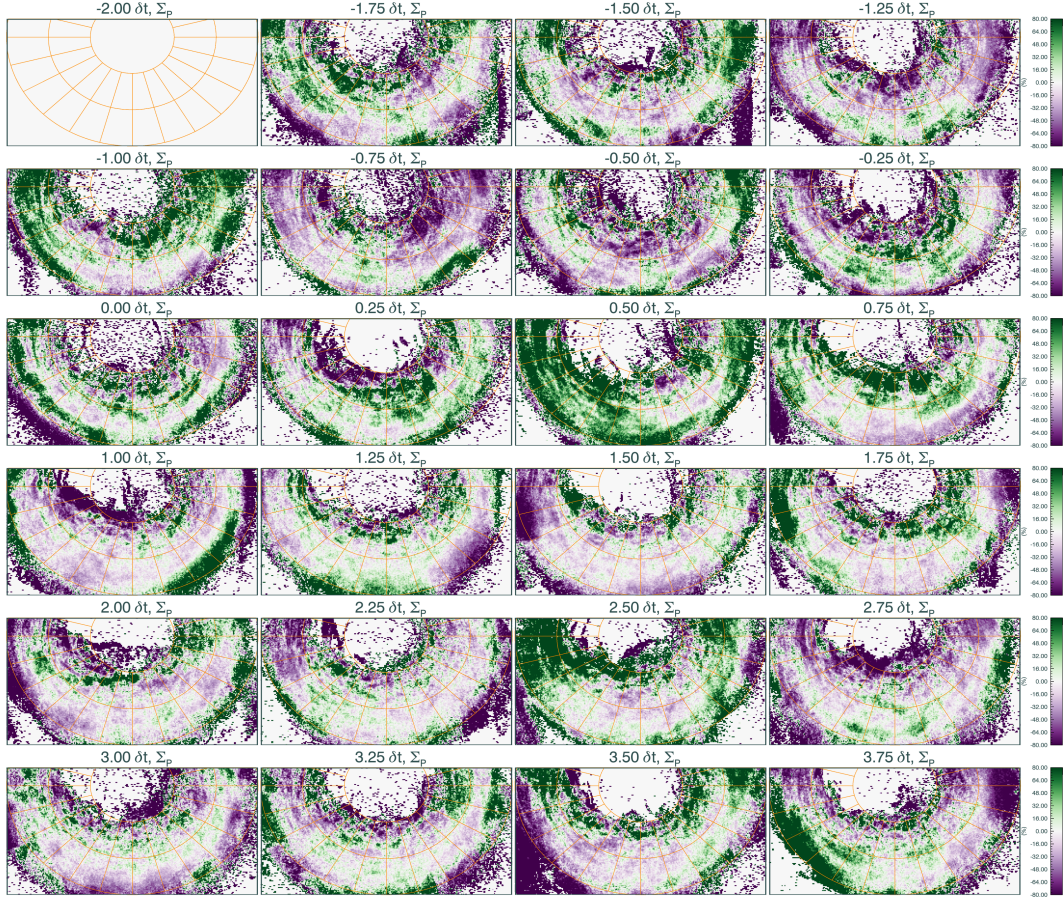


**Figure 4.** A series of images showing the percentage difference in Pedersen conductance from the previous normalised-time step, for substorm onsets that occur between  $63^\circ$  to  $65^\circ$  degrees magnetic latitude. The orientation and organisation of the plots is as in Fig. 3

MLT = 23 hr and MLT = 00 hr show a rapid reduction to levels similar to the other MLT sectors by  $2\delta t$  or by 1.5 hr after onset.

We now explore the behavior of various parameters over the course of an average substorm, at all substorm onset magnetic latitude bins. In Fig. 6 we plot a set of time series with each step a multiple of  $\delta t$  as defined in Section 2. Each latitude bin is colored according to the legend given in the plot. Parameters from the SSUSI stacked data have been averaged over a wedge shape, within a MLT range of 21 hrs to 02 hrs and at co-latitudes less than  $30^\circ$  to encompass the auroral bulge. We plot a time series of the mean energy ( $E_0$ ), energy flux ( $Q$ ), and ratio between  $Q$  and  $E_0$ , the mean height-integrated Hall then Pedersen conductance, and then the mean Pedersen conductance offset from the mean conductance in the time period from  $-2\delta t$  to  $-0.5\delta t$ , i.e. prior to onset. We also plot the mean up and down FAC densities, taken from all contributing individual values in a given spatial wedge shape. These values are averaged over all latitudes, but taken in a narrow MLT sector between 4 hr and 5 hr MLT to encompass the maxima of the region 2 FACs in the post midnight sector. The spatial selection applied here extracts region 2 upwards FAC and region 1 downwards FAC.

In Fig. 6 (a)-(b) and (d)-(e), we observe that  $E_0$ , and  $Q$ , and the conductances are broadly ordered by magnetic latitude of onset. The peak parameter values are for the second to lowest magnetic latitude substorms occurring between  $63^\circ$  to  $65^\circ$ . Hall and Pedersen conductances peak at nearly 11 mho and 5 mho, respectively, for the  $63^\circ$  to  $65^\circ$  bin. All parameter values decrease with increasing magnetic latitude, although the highest latitude bins over  $71^\circ$  are almost indistinct from one another.  $E_0$  increases after onset, reaching a maximum of  $\approx 3.5$  keV within  $1.25\delta t$  after onset, with the exception of the lowest latitude substorms of  $50^\circ$  to  $63^\circ$ , which is slower to ramp up and peaks at  $1.75\delta t$  at 3.2 keV. At the majority of these energies, the Gaussian assumption used in the SSUSI data set gives lower Pedersen conductances as compared to the Maxwellian assumption. An increase in  $Q$  is observed by  $1\delta t$  after onset, peaking at  $4.3 \text{ ergs cm}^{-2} \text{ s}^{-1}$ . The  $63^\circ$  to  $65^\circ$  substorms parameter values remain elevated after onset for the whole normalised-time period shown ( $4\delta t$ ). To a lesser extent, this slow delay in recovery to pre-substorm values is also seen in magnetic latitude bins  $50^\circ$  to  $63^\circ$  and  $65^\circ$  to  $67^\circ$ . Changes in  $E_0$ , and  $Q$  are largest and slower to recover for the lowest magnetic latitude bins, which is consistent with Grocott et al. (2009) and Milan et al. (2009) who showed that lower-latitude onset substorms, with onsets at magnetic latitudes less than  $65^\circ$ , produced brighter aurora that also persisted for longer. Following a detailed study of a substorm using precise but spatially constrained incoherent scatter radar measurements, Lester et al. (1996) inferred an increase in precipitating particle energy to more than 10 keV during the substorm recovery phase, or post  $1\delta t$  in comparison to the time series here, whereas they observed that the expansion phase mean energy remained fairly constant at approximately 2.5 keV. This was for one substorm, detected by a set of magnetometers between  $63.6^\circ$  and  $67.3^\circ$  magnetic latitude, and the mean energy here is slightly lower than 2 keV prior to onset for magnetic latitudes between  $65^\circ$  to  $67^\circ$ . Here, we see an increase in precipitating energy before the recovery phase starts at  $1\delta t$ , but a peak in energy after  $1\delta t$  to more modest mean energies up to a maximum of 3.6 keV, although here we average over a wide range of magnetic local times.

Fig. 6 (c) shows the mean ratio between  $Q$  and  $E_0$  during a substorm. This ratio gives an indication of the number of precipitating particles. Most magnetic latitude bins, exhibit a slight rise in the ratio from substorm onset at about  $1.3 \text{ erg cm}^{-2} \text{ s}^{-1} \text{ keV}^{-1}$  to a maximum of  $1.8 \text{ erg cm}^{-2} \text{ s}^{-1} \text{ keV}^{-1}$ , an increase of approximately 40%, which lasts until approximately  $1.25\delta t$  interval post onset. The highest latitude bin, for onsets above  $73^\circ$ , only sees an increase  $0.5\delta t$  after onset, but then shows a large variation in the ratio. Similarly, the lowest latitude bin  $50^\circ$  and  $63^\circ$ , shows large variations in the ratio from  $1.75\delta t$ . Both these bins have the lowest number of contributing substorm onsets, and may show the largest variation in substorm duration. Given the flatter changes in  $E_0$  as com-

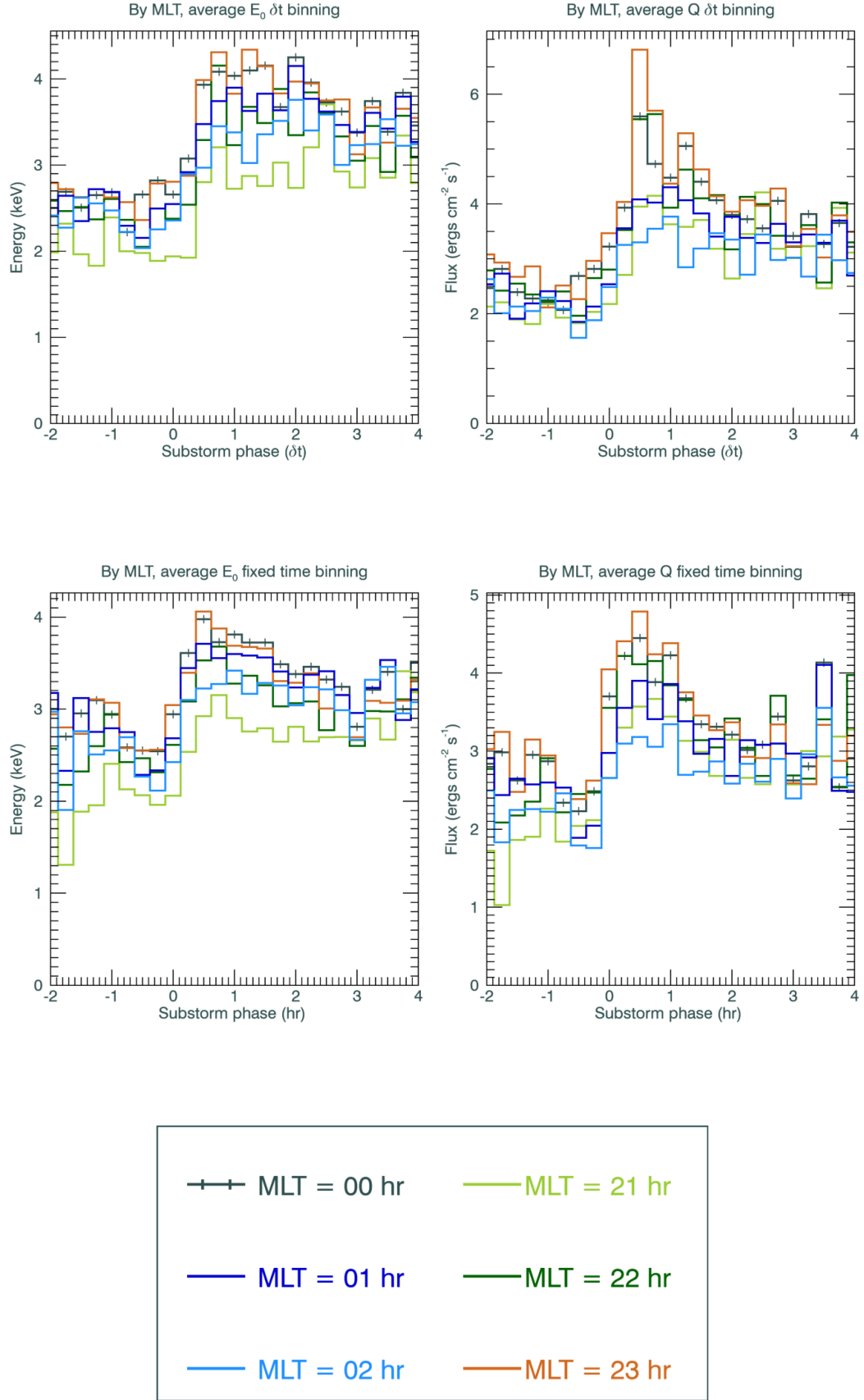


**Figure 5.**  $E_0$  and  $Q$  over the course of a substorm by MLT, for substorms with onsets that occur between  $63^\circ$  to  $65^\circ$  degrees magnetic latitude. The top row is for the  $\delta t$ -defined time grid, and the bottom row for the fixed time binning.

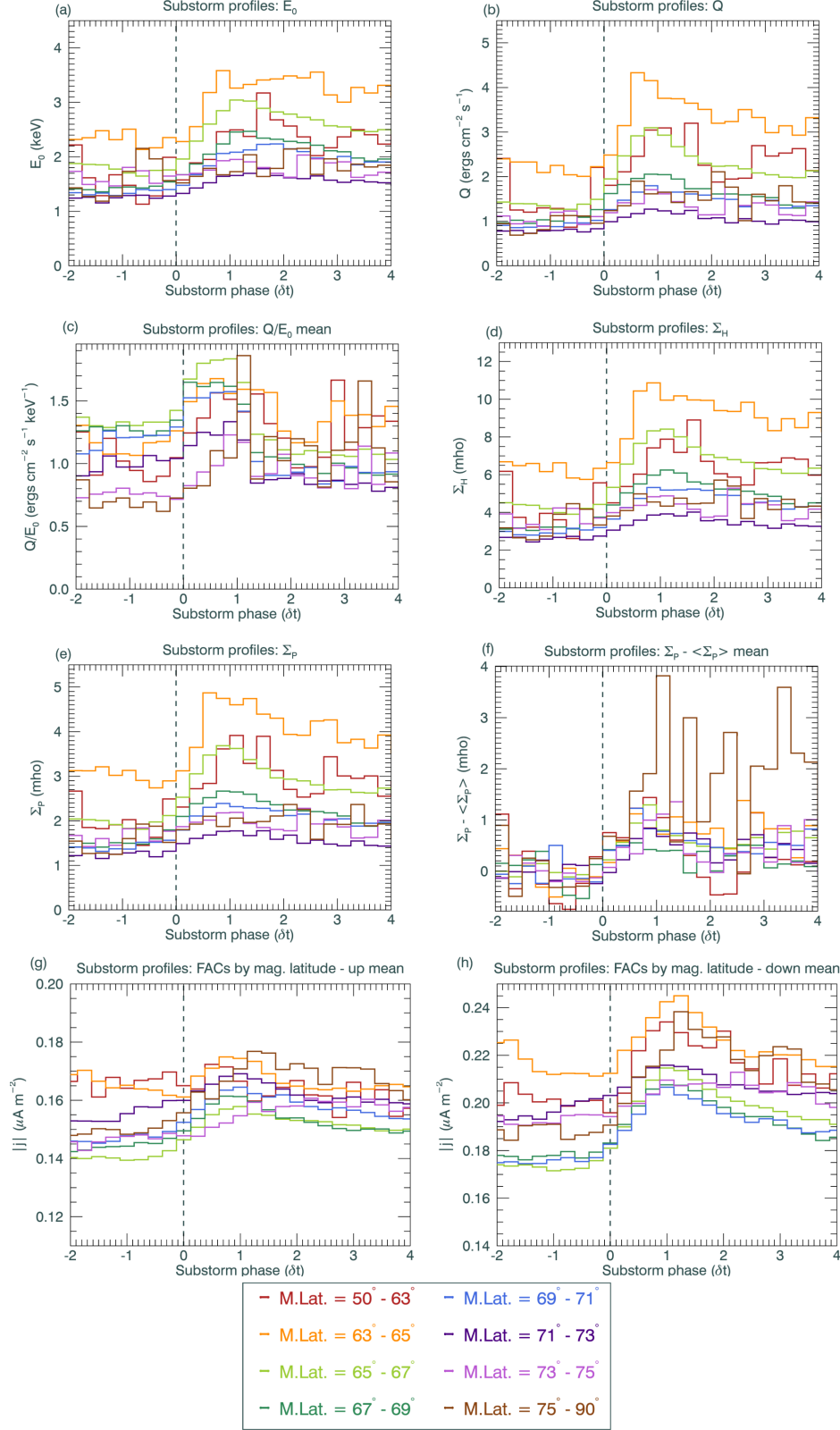


**Figure 6.** Adjusted time series of various quantities versus the  $\delta t$  defined step of an average substorm, by magnetic latitude bin, averaged over a restricted 21 hrs to 02 hrs MLT sector and down to latitudes of  $30^\circ$ . Panels (a) - (c):  $E_0$ , then  $Q$ , and the ratio between them. Panels (d) - (f): Hall, and Pedersen mean height-integrated conductances, followed by the Pedersen conductance adjusted by the mean from  $2\delta t$  to  $0.5\delta t$  prior to onset. Panels (g) and (h): timeseries for average up, and then down FACs in a narrow MLT wedge, parameterised by magnetic latitude as the other parameters, over the course of an average substorm. A key to the color scheme is shown bottom right. Dashed vertical lines mark onset.



pared to  $Q$ , it appears that increases in mean energy flux  $Q$  at substorm onset is driving changes after the recovery phase at  $1 \delta t$ , rather than any marked difference in the mean energy of the precipitating particles. We explore this issue in our discussion below.

In Fig. 6 (f), shows the Pedersen conductance offset from the average Pedersen conductance between  $2 \delta t$  and  $0.5 \delta t$  prior to onset. This plot reduces any biases in the data that may exist as the result of geomagnetic storms whereby large conductances prior to onset may influence our results. However, as we see no magnetic latitudinal dependence here, large geomagnetic storms do not appear to be causing any biases in the previous panels. The SOPHIE list uses the SuperMAG SML index in finding onsets. In the event of a large geomagnetic storm resulting in a long period decrease in the SML index, the SOPHIE technique is unlikely to find multiple instances of substorms occurring within an overall downward trend in SML. The highest latitude bin over  $75^\circ$  shows elevated values above the mean after onset, and is likely to reflect weaker storms with a larger variety of durations. Substorms within lower-latitudinal ranges are likely to have a longer duration. Milan et al. (2019, and references therein) explored convection braking for substorm with low-latitude onsets, and they quote a threshold of  $65^\circ$  magnetic latitude, above which convection braking is unlikely to occur. Onsets which start below  $65^\circ$  magnetic latitude are likely to have a more intense auroral response, leading to enhanced conductance (e.g. in panel (e)) in the auroral bulge, which arrests the convection flow. We make no selection based on a minimum time between substorm onsets in our processing steps, and so our data set may include sawtooth events whereby a substorm-like signature is seen to repeat approximately every 3 hours (Borovsky et al., 1993), although these are rare phenomena occurring during enhanced geomagnetic activity (Walach & Milan, 2015).

In Fig. 6 (g) and (h), the upwards FACs show less clear behavior over the course of a substorm than the downwards FACs. We note a slow increase in the magnitude of the average upwards current building up to a maximum at  $1 \delta t$ , for the majority of the magnetic latitude bins. The largest current magnitudes are seen for the  $63^\circ$  to  $65^\circ$  and  $75^\circ$  to  $90^\circ$  magnetic latitude bin. One exception occurs for the lowest bin of onsets, from  $50^\circ$  to  $63^\circ$  which shows elevated average upwards current magnitudes prior to onset, which decrease after onset. Also, the bin from  $73^\circ$  to  $75^\circ$  shows a delayed and a very slow ramp up to the peak in the average upwards current magnitudes after more than  $2 \delta t$ . The upwards FAC in the narrow MLT sector used for this time series represent region 2 FACs. Region 1 FACs have been shown to have higher current magnitudes compared to region 2 FACs by about 20 % within 1 hour of onset on average (Coxon et al., 2014). We see in excess of 20 % greater FAC current magnitude between region 2 and region 1 (downwards) FACs here.

The downwards, or region 1, FACs, do show a clearer ordering by magnetic latitude into two regimes, with the exception of the highest latitude onsets above  $75^\circ$ . Those for the lowest latitude bins, ranging from  $50^\circ$  to  $65^\circ$  magnitudes show much large average downwards currents magnitudes than the other magnetic latitude bins, which in turn, show very little dependence on latitude above  $65^\circ$ . All magnetic latitude bins show an increase in current magnitude after onset, peaking in the main around  $1 \delta t$ . The current magnitudes recover similarly, and slowly between latitude bins after onset.

In Fig. 7 we show histograms of all the contributing or calculated values from the SSUSI and AMPERE data sets; for  $E_0$ ,  $Q$ , Hall and Pedersen conductances, and the FACs split into up, red, and down, blue, currents. The FACs are given for the whole data set, regardless of substorm onset latitude.  $E_0$  is limited to 20 keV through the SSUSI data processing procedures, and the distribution by energy is not dependent on the magnetic latitude of onset. The  $Q$  values show a separation by substorm onset magnetic latitude, whereby the  $63^\circ$  to  $65^\circ$  magnetic latitude bin exhibits the highest values of  $Q$ , and across all  $Q$  this latitude bin has a larger number of contributing points. Therefore we postulate that enhanced conductances for substorms occurring between magnetic latitudes of

63° to 65° appear driven by increased flux, rather than an increase in the energy of precipitating particles. Individual Hall and Pedersen conductances, calculated from individual pixel measurements, can peak at over 200 mho or 60 mho respectively.

In Fig. 8 we plot a similar set of panels as for Fig. 6, but instead of using the  $\delta t$  time step, calculated for each contributing substorm individually, we use a simple fixed time step of 0.25 hours to perform the superposed epoch analysis.

The fixed binning time series shows similar behavior to that based on  $\delta t$ . The magnetic latitude bin with the largest values of  $E_0$  and  $Q$  at substorm onset is 63° to 65°, as before for the  $\delta t$  grid. The lowest magnetic latitude bin, for 50° to 63° is the most erratic. The large values at the beginning and end of the substorm period around 2 hr prior or beyond 3 hr after onset may indicate that after this time it is likely that a second substorm had occurred so that at the extremes of the time series overlapping substorms are being detected. The remaining bins are ordered by magnetic latitude, whereby the largest parameter values seen for the lowest magnetic latitude onsets, as seen previously. As before, parameters peak before 1 hour after onset. FAC magnitudes for these fixed bins are strongest for the lowest three latitude bins, as seen previously, and again this is most apparent for the downwards (region 1) FACs. Here, the 63° to 65° current magnitudes are largest by some margin, for both upwards and downwards FACs.

The normalisation of the substorms to  $\delta t$ , defined as the duration of the expansion phase, that we used in this work may still hide features of the progression of a substorm. In this paper, we normalise the time series to multiples of  $\delta t$ . The modal  $\delta t$  value is shown in Fig. 1 to between 0.10 and 0.20 hr, or 6 to 12 minutes. Walach et al. (2017) made a statistical study of substorms using images of ultraviolet aurora, and saw the expansion phase typically lasting from 10 to 20 minutes after onset of the electron aurora, so therefore we justify the use of the independently calculated  $\delta t$  for binning of the conductances, derived from auroral data, in this paper. It is not necessarily the case that a longer total-duration substorm will have a longer expansion phase, nor is it true that conversely, shorter total-duration substorms have shorter expansion phases. The end of the recovery phase, when the auroral electrojet lower envelope boundary returns to a quiescent state and which would enable the calculation of the overall duration of each substorm, is not stored in the Forsyth et al. (2015) list. Walach et al. (2017) observed the recovery phase to occur by 50 minutes post onset for the electron aurora, which for a modal  $\delta t$  of 0.15 hr equates to 1.25  $\delta t$ . We see a peak in parameter values starting before 1  $\delta t$ , but a slow recovery to values prior to onset. Smearing of the data will inevitably occur over either the  $\delta t$  or fixed-time grid. Even so, the binning used in this paper is able to order the height-integrated conductances,  $E_0$ ,  $Q$ , and region 1 downwards FACs by magnetic latitude of onset.

The dominance of high-parameter values for substorms with onsets that occur between 63° to 65° magnetic latitude is still to be determined. The influence of the ring current modulating tail reconnection and arresting substorm onset may play a part (Milan et al., 2021). We leave this to future investigation.

## 4 Conclusions

We have examined the behavior of mean energy, mean energy flux, and height-integrated conductances over the course of a substorm, using a superposed epoch analysis of auroral emissions derived parameters. We examined the behavior on both an artificial, normalised-time grid based on the duration of the expansion phase, and a fixed time grid. Average substorm timeseries are found for a set separated by the magnetic latitude of substorm onset into broad bins of different widths between 50° to approximately 80°. For both normalised and fixed time grids, the maximum parameter values were observed for onsets that occur between 63° to 65° magnetic latitude. Why this latitude bin shows larger parameter values is still to be determined. Changes in the mean energy flux shortly af-

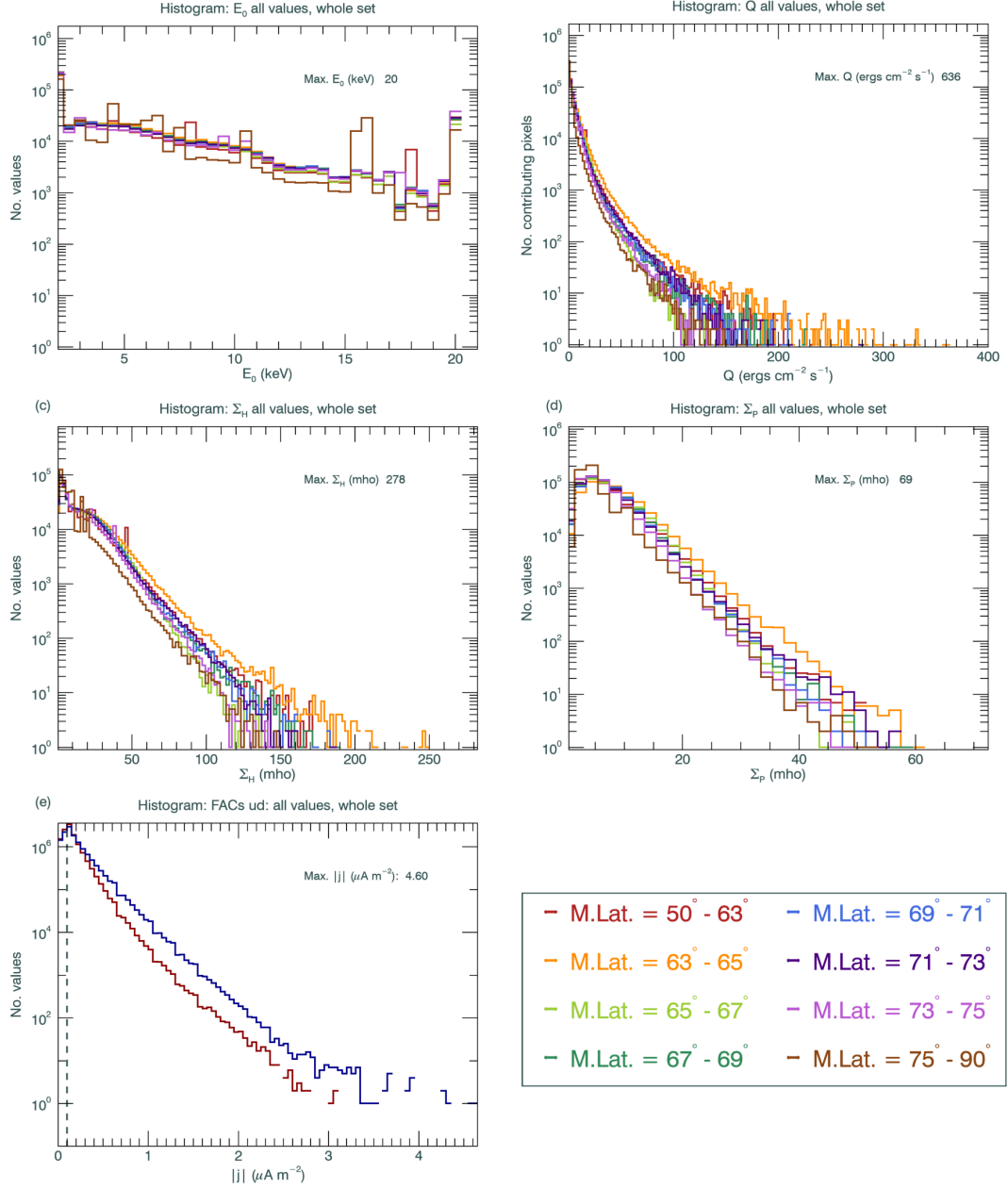


**Figure 7.** A set of histograms showing the distribution of all contributing data parameters for  $E_0$ ,  $Q$ , Hall and Pedersen conductances, and the FACs split into up, red, and down, blue, currents. The  $Q$  panel has a restricted x-axis range to better show differences between magnetic latitude bins. The dashed line in (e) shows the threshold current density applied to the AMPERE data set.

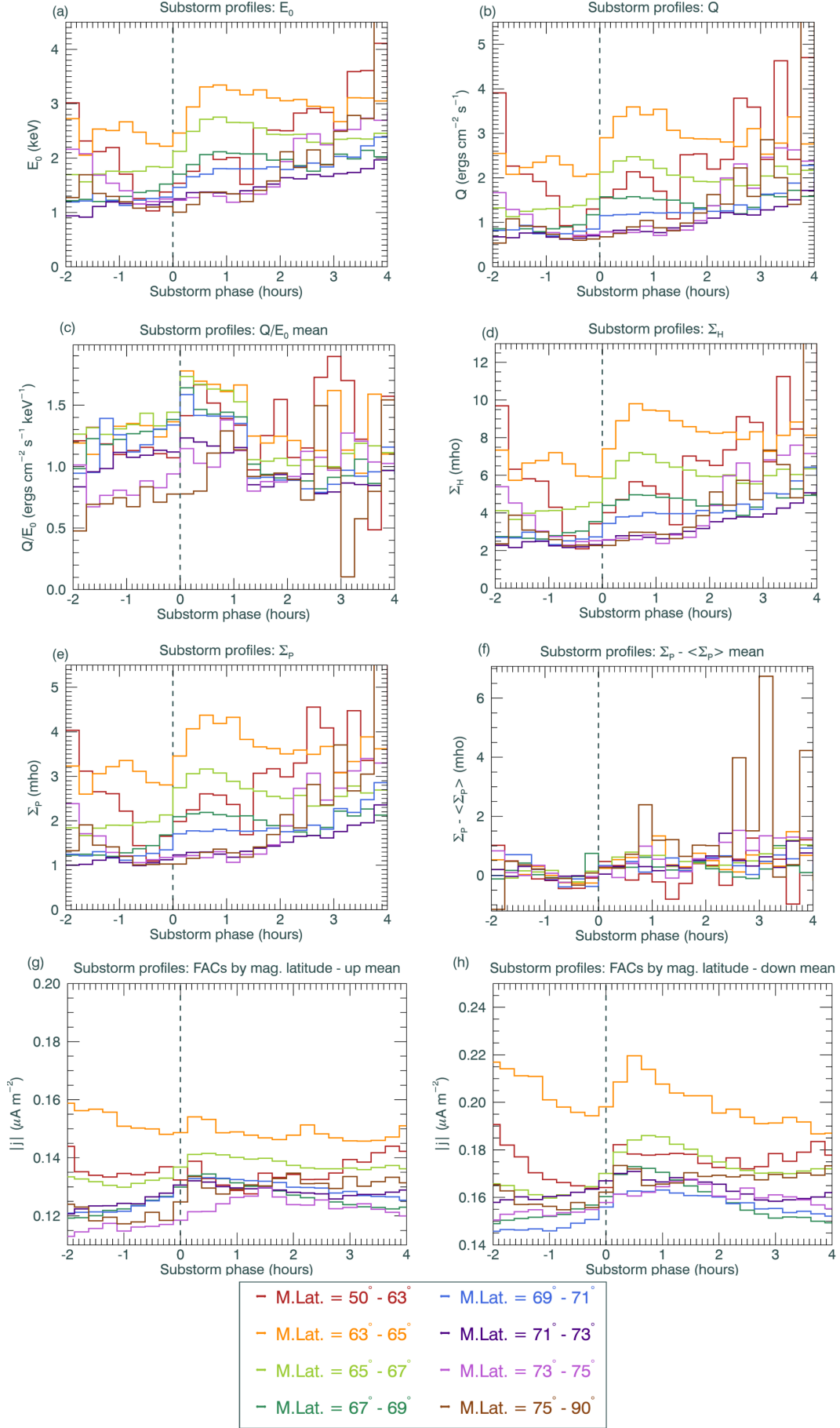


**Figure 8.** A set of time series in the same layout as Fig. 6, but using a fixed time step of 0.25 h for the superposed epoch analysis.

ter substorm onset are greater than changes in the mean energy of the precipitation. Higher magnetic latitude onsets exhibit lower values, throughout an entire substorm. For the normalised time binning, magnetic latitude onsets behave similarly over the course of a substorm, with values peaking by the start of the recovery phase, and decaying afterwards. Lower latitude onset parameters decay slower to their pre-onset values than high latitude onsets. The fixed time binning series are likely to include several overlapping substorms, which affects the lowest magnetic latitude bin the most. FACs respond to a substorm in a similar manner to the auroral parameters, and this is most apparent in the downwards current magnitudes. FAC current magnitudes are also ordered by magnetic latitude, so that the lower magnitude latitude onsets exhibit the highest current magnitudes.

This work uses auroral emissions that are obtained by low-altitude spacecraft observing the ionosphere from above, with the advantage of observing large areas of the polar cap over short durations. Future work will involve comparing the wide-field aurora-derived parameters with those obtained incoherent radar data taken from ground-based facilities to verify the technique in a spatially constrained region.

## 5 Open Research

The DMSP/SSUSI file type EDR-AUR data were obtained from <http://ssusi.jhuapl.edu> (data version 0106, software version 7.0.0, calibration period version E0018). AMPERE data were obtained from <http://ampere.jhuapl.edu>. The AMPERE-derived region 1 region 2 FAC radii are stored at <https://doi.org/10.25392/leicester.data.11294861.v1>. SuperMAG data can be found via the portal at <http://supermag.jhuapl.edu>.

## Acknowledgments

JAC and SEM gratefully acknowledge support from the Science Technology Facilities Council (STFC) consolidated grant ST/N000429/1, and JAC additionally acknowledges the grant from the Royal Society DHF\R1\211068. M.-T. W. gratefully acknowledges support from the Natural Environments Research Council (NERC) UK, grant number NE/T000937/1. This research used the ALICE and SPECTRE High Performance Computing Facility at the University of Leicester.

## References

- Anderson, B. J., Takahashi, K., & Toth, B. A. (2000). Sensing global Birkeland currents with iridium® engineering magnetometer data. *Geophys. Res. Letter.*, 27, 4045-4048. doi: 10.1029/2000GL000094
- Borovsky, J. E., Nemzek, R. J., & Belian, R. D. (1993, March). The occurrence rate of magnetospheric-substorm onsets: Random and periodic substorms. *Journal of Geophysical Research*, 98(A3), 3807-3814. doi: 10.1029/92JA02556
- Carter, J. A., Milan, S. E., Paxton, L. J., Anderson, B. J., & Gjerloev, J. (2020). Height-integrated ionospheric conductances parameterized by interplanetary magnetic field and substorm phase. *Journal of Geophysical Research: Space Physics*, 125(10), e2020JA028121. Retrieved from <https://agupubs.onlinelibrary.wiley.com/doi/abs/10.1029/2020JA028121> (e2020JA028121 10.1029/2020JA028121) doi: <https://doi.org/10.1029/2020JA028121>
- Clausen, L. B. N., Baker, J. B. H., Ruohoniemi, J. M., Milan, S. E., & Anderson, B. J. (2012, June). Dynamics of the region 1 Birkeland current oval derived from the Active Magnetosphere and Planetary Electrodynamics Response Experiment (AMPERE). *Journal of Geophysical Research (Space Physics)*, 117, 6233. doi: 10.1029/2012JA017666

- Coxon, J., Milan, S., Clausen, L., Anderson, B., & Korth, H. (2014). The magnitudes of the regions 1 and 2 birkeland currents observed by ampere and their role in solar wind-magnetosphere-ionosphere coupling. *Journal of Geophysical Research: Space Physics*.
- Denton, M. H., Borovsky, J. E., Stepanova, M., & Valdivia, J. A. (2016). Preface: Unsolved problems of magnetospheric physics. *Journal of Geophysical Research: Space Physics*, 121(11), 10,783-10,785. Retrieved from <https://agupubs.onlinelibrary.wiley.com/doi/abs/10.1002/2016JA023362> doi: 10.1002/2016JA023362
- Forsyth, C., Rae, I. J., Coxon, J. C., Freeman, M. P., Jackman, C. M., Gjerloev, J., & Fazakerley, A. N. (2015). A new technique for determining substorm onsets and phases from indices of the electrojet (sophie). *Journal of Geophysical Research: Space Physics*, 120(12), 10,592-10,606. Retrieved from <https://agupubs.onlinelibrary.wiley.com/doi/abs/10.1002/2015JA021343> doi: <https://doi.org/10.1002/2015JA021343>
- Gjerloev, J. W. (2012). The supermag data processing technique. *Journal of Geophysical Research: Space Physics*, 117(A9). Retrieved from <https://agupubs.onlinelibrary.wiley.com/doi/abs/10.1029/2012JA017683> doi: 10.1029/2012JA017683
- Gjerloev, J. W., Hoffman, R. A., Sigwarth, J. B., & Frank, L. A. (2007). Statistical description of the bulge-type auroral substorm in the far ultraviolet. *Journal of Geophysical Research: Space Physics*, 112(A7). Retrieved from <https://agupubs.onlinelibrary.wiley.com/doi/abs/10.1029/2006JA012189> doi: 10.1029/2006JA012189
- Grocott, A., Wild, J. A., Milan, S. E., & Yeoman, T. K. (2009). Superposed epoch analysis of the ionospheric convection evolution during substorms: onset latitude dependence. *Annales Geophysicae*, 27(2), 591-600. Retrieved from <https://angeo.copernicus.org/articles/27/591/2009/> doi: 10.5194/angeo-27-591-2009
- Lam, M. M., Freeman, M. P., Jackman, C. M., Rae, I. J., Kalmoni, N. M. E., Sandhu, J. K., & Forsyth, C. (2019, April). How Well Can We Estimate Pedersen Conductance From the THEMIS White-Light All-Sky Cameras? *Journal of Geophysical Research (Space Physics)*, 124(4), 2920-2934. doi: 10.1029/2018JA026067
- Lester, M., Davies, J. A., & Viridi, S. (1996, Dec). High-latitude Hall and Pedersen conductances during substorm activity in the SUNDIAL-ATLAS campaign. *Journal of Geophysical Research*, 101(A12), 26719-26728. doi: 10.1029/96JA00979
- McGranaghan, R., Knipp, D. J., Matsuo, T., Godinez, H., Redmon, R. J., Solomon, S. C., & Morley, S. K. (2015). Modes of high-latitude auroral conductance variability derived from dmsp energetic electron precipitation observations: Empirical orthogonal function analysis. *Journal of Geophysical Research: Space Physics*, 120(12), 11,013-11,031. Retrieved from <https://agupubs.onlinelibrary.wiley.com/doi/abs/10.1002/2015JA021828> doi: 10.1002/2015JA021828
- Milan, S. E., Carter, J. A., Sangha, H., Bower, G. E., & Anderson, B. J. (2021, February). Magnetospheric Flux Throughput in the Dungey Cycle: Identification of Convection State During 2010. *Journal of Geophysical Research (Space Physics)*, 126(2), e28437. doi: 10.1029/2020JA028437
- Milan, S. E., Carter, J. A., Sangha, H., Laundal, K. M., Østgaard, N., Tenfjord, P., ... Anderson, B. J. (2018, September). Timescales of Dayside and Nightside Field-Aligned Current Response to Changes in Solar Wind-Magnetosphere Coupling. *Journal of Geophysical Research (Space Physics)*, 123(9), 7307-7319. doi: 10.1029/2018JA025645
- Milan, S. E., Grocott, A., Forsyth, C., Imber, S. M., Boakes, P. D., & Hubert,



- B. (2009, February). A superposed epoch analysis of auroral evolution during substorm growth, onset and recovery: open magnetic flux control of substorm intensity. *Annales Geophysicae*, 27(2), 659-668. doi: 10.5194/angeo-27-659-2009
- Milan, S. E., Walach, M.-T., Carter, J. A., Sangha, H., & Anderson, B. J. (2019). Substorm onset latitude and the steadiness of magnetospheric convection. *Journal of Geophysical Research: Space Physics*, 124(3), 1738-1752. Retrieved from <https://agupubs.onlinelibrary.wiley.com/doi/abs/10.1029/2018JA025969> doi: 10.1029/2018JA025969
- Mukhopadhyay, A., Welling, D. T., Liemohn, M. W., Ridley, A. J., Chakraborty, S., & Anderson, B. J. (2020, November). Conductance Model for Extreme Events: Impact of Auroral Conductance on Space Weather Forecasts. *Space Weather*, 18(11), e02551. doi: 10.1029/2020SW002551
- Newell, P. T., & Gjerloev, J. W. (2011, December). Evaluation of SuperMAG auroral electrojet indices as indicators of substorms and auroral power. *Journal of Geophysical Research (Space Physics)*, 116(A15), 12211. doi: 10.1029/2011JA016779
- Paxton, L. J., & Anderson, D. E. (1992). Far ultraviolet remote sensing of Venus and Mars. *Washington DC American Geophysical Union Geophysical Monograph Series*, 66, 113-189. doi: 10.1029/GM066p0113
- Paxton, L. J., & Zhang, Y. (2016). *Far ultraviolet imaging of the aurora. In Space Weather Fundamentals*. CRC press.
- Robinson, R. M., Vondrak, R. R., Miller, K., Dabbs, T., & Hardy, D. (1987). On calculating ionospheric conductances from the flux and energy of precipitating electrons. *Journal of Geophysical Research: Space Physics*, 92(A3), 2565-2569. Retrieved from <https://agupubs.onlinelibrary.wiley.com/doi/abs/10.1029/JA092iA03p02565> doi: 10.1029/JA092iA03p02565
- Walach, M. T., & Milan, S. E. (2015, March). Are steady magnetospheric convection events prolonged substorms? *Journal of Geophysical Research (Space Physics)*, 120(3), 1751-1758. doi: 10.1002/2014JA020631
- Walach, M.-T., Milan, S. E., Murphy, K. R., Carter, J. A., Hubert, B. A., & Grocott, A. (2017). Comparative study of large-scale auroral signatures of substorms, steady magnetospheric convection events, and sawtooth events. *Journal of Geophysical Research: Space Physics*, 122(6), 6357-6373. Retrieved from <https://agupubs.onlinelibrary.wiley.com/doi/abs/10.1002/2017JA023991> doi: 10.1002/2017JA023991
- Waters, C. L., Anderson, B. J., & Liou, K. (2001). Estimation of global field aligned currents using the iridium® system magnetometer data. *Geophys. Res. Letter.*, 28, 2165-2168. doi: 10.1029/2000GL012725